<Supplementary Information>

In situ crystal reconstruction strategy based highly efficient air-processed inorganic $CsPbI_2Br$ perovskite photovoltaics for indoor, outdoor, and switching applications

Jitendra Bahadur [a], Jun Ryu [b], Padmini Pandey [a], SungWon Cho [b], Jung Sang Cho [c] and Dong-Won Kang [a, b, †]

[a] Department of Energy Systems Engineering, Chung-Ang University, Seoul, 06974 Republic of Korea

[b] Department of Smart City, Chung-Ang University, Seoul, 06974 Republic of Korea

[c] Department of Engineering Chemistry, Chungbuk National University, 1 Chungdae-Ro, Seowon-Gu, Cheongju-si, Chungbuk 361-763, Republic of Korea

† Corresponding authors: D.-W. Kang: kangdwn@cau.ac.kr

J.S. Cho: jscho@cbnu.ac.kr

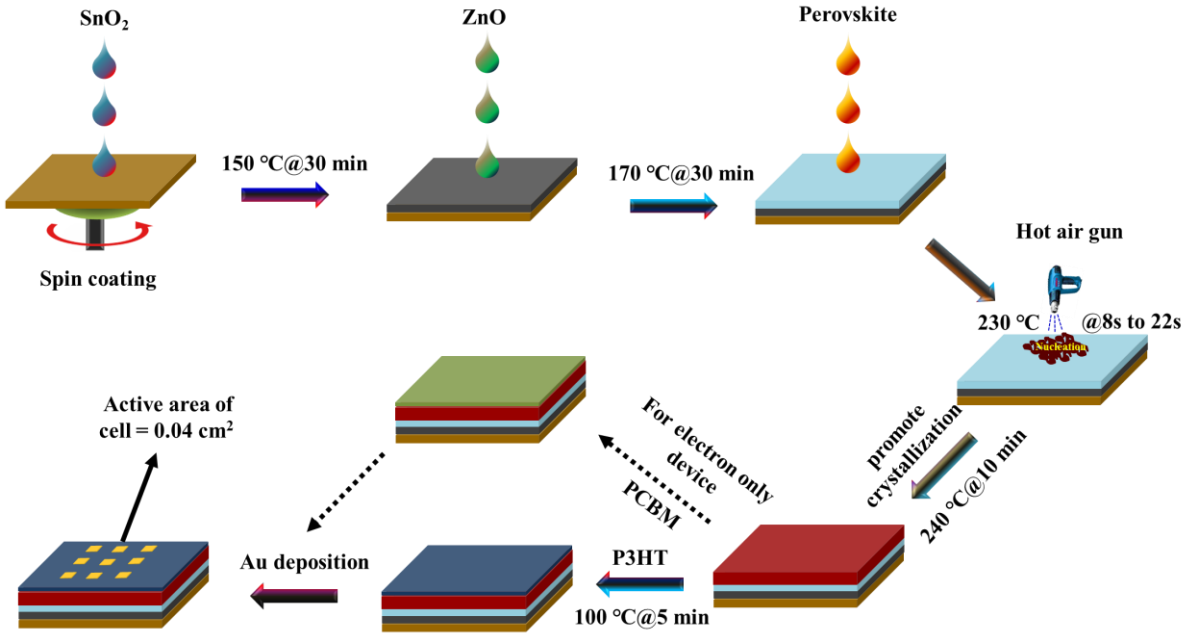

Fig. S1 Schematic representation of device fabrication.

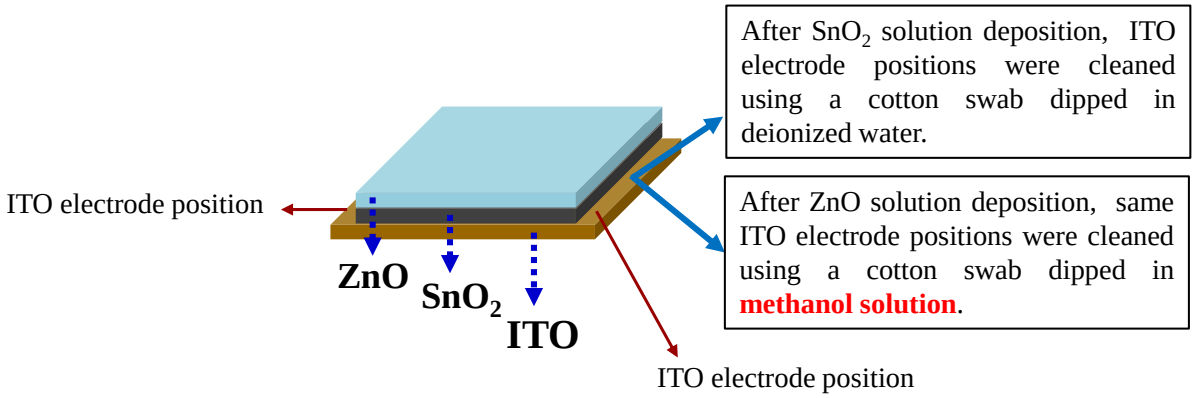

Fig. S2: Schematic representation for use of methanol solution.

Procedure of dynamic hot air treatment: Before spin coating of perovskite solution, first set the hot air gun temperature at 230 °C and turned on the hot air gun. Then, drop the perovskite precursor solution on ZnO/SnO_2/ITO substrate and start the spin coating process (3000 rpm for 40 s) as shown in Fig. S3. After spinning of 8 s, dynamic hot air treatment was performed using hot air gun (230 °C) by keeping ~ 2 cm distance from substrate up to 22 s continuously and then completed the spin coating process. Afterward, substrate was transferred to hot plate and annealed at 240 °C for 10 min to form α-CPIB active phase.

Specific parameters related to hot air gun treatment: We have bought hot air gun from Bosch company (Bosch, GHG 630 DCE hot air gun - 0601 94C 740), Temperature of hot air gun was 230 °C during dynamic hot air treatment, and distance of hot air gun from substrate is ~ 2 cm during dynamic hot air treatment.

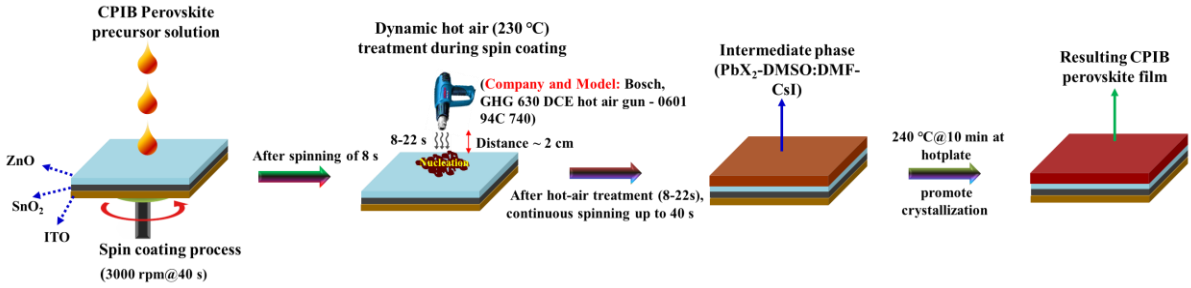

Fig. S3: Schematic representation for fabrication of perovskite film using dynamic hot air process.

Characterization Techniques

Crystallographic analysis

To investigate the present phase and crystallinity of the prepared perovskite films, XRD patterns were recorded using X-ray diffractometer (Bruker-AXS, D8-Advance) with Cu Kα radiation, where λ = 1.54 Å). The XRD parameters, such as the average crystallite size, microstrain, and dislocation density, were calculated using Debye–Scherrer formula and Hall–Williamson equation, as demonstrated in the main manuscript.

Morphological analysis

The top surface images of perovskite films were captured using field emission scanning electron microscopy (FE-SEM; Carl Zeiss, AURIGA) to examine microstructural properties.

Optical analysis

The absorption patterns were measured using ultraviolet-visible spectroscopy (UV-2700, Shimadzu), and photoluminescence (PL) spectra were recorded with a 495 nm laser excitation wavelength using a spectrofluorometer (FP-8600, Jasco) corresponding to the perovskite films to examine the optoelectronic properties.

Elemental analysis

The x-ray photoelectron spectroscopy (XPS) patterns were obtained through the K-Alpha^{+} system with monochromatic Al Kα x-ray radiation (photon energy = 1486.6 eV) under a high vacuum (~5 x 10^{-8} Torr) to identify the chemical bonding states.

Fourier transform infrared (FTIR) analysis

The FTIR patterns were measured using Thermo Scientific Nicolet 6700 spectrometer.

Photovoltaic analysis under indoor/outdoor lighting conditions

The current density voltage (J-V) curves for fabricated PSCs were recorded under AM 1.5 illumination (100 mW/cm^2) using a solar simulator (Peccell Technologies, PEC-L01) with a scanning rate of 0.25 V/s. The AM 1.5 solar simulator light intensity was adjusted to 100 mW/cm^2 using a reference silicon solar cell. The EQE spectrums were measured using a monochromator (DongWoo Optron, MonoRa500i) with a power source (Xenon lamp 150 W, Abet Technologies, 13,014). For indoor light performance, the J-V curves were measured under LED (3200 K) lighting conditions at 1000 lux with a corresponding power of 382 μW/cm^2 to calculate the indoor PCE.

Charge carrier transport and recombination analysis

The space charge limited current (SCLC) patterns were obtained with an electron-only device architecture (ITO/SnO_2/ZnO/Perovskite/PCBM/Au) under dark conditions using a Keithley-2400 source meter. The electrochemical impedance spectroscopy spectrums were recorded using CompactStat (Ivium Technologies) with frequency ranges of 2 MHz to 1 Hz and an applied bias voltage of 1.0 V under dark conditions, and the curves were fitted using Zview software. The transient photocurrent (TPC) and transient photovoltage (TPV) decays were measured using multifunctional organic semiconductor parameter system (Mcscience, T400) containing a Tektronix digital phosphor oscilloscope with a 100 MHz bandwidth (DPO-2014B).

Stability analysis

The air stability of perovskite films was monitored in ambient conditions (relative humidity: 45%, temperature: ~22.8 ℃) at different time intervals. The thermal stability of the devices was measured in a dry box at 85 ℃ over 720 h. The performance of the PSCs was measured periodically using an AM 1.5 solar simulator with light illumination (100 mW/cm^2) under ambient conditions.

All these measurements for perovskite films and devices were performed in an ambient environment (relative humidity range: 40% ~ 48%, temperature: 21~ 26 ℃).

Role of 4-tertbutylpyridine (tBP) additive into P3HT perovskite precursor:

The poly(3-hexylthiophene) (P3HT) was extensively used as hole transport material (HTM) in the fabrication of perovskite solar cells due to its unique properties such as wide optical band gap, low production cost, thermal stability, good solubility in variable solvents, etc [S1-4]. However, P3HT has low hole mobility owing to poor crystalline feature [S4], causes charge carrier recombination at HTL/perovskite interface, resulting degrade the device performance. To overcome this issue, various research groups suggested that 4-tertbutylpyridine (tBP) dopant with P3HT improves hole selectivity at HTL/perovskite interface [S1], increases packing and crystallinity [S5], enhances charge carrier mobility by improvement of the polymer chain ordering [S1,2], significantly reduced the trap assisted charge recombination and hence leading to higher photovoltaic performance.

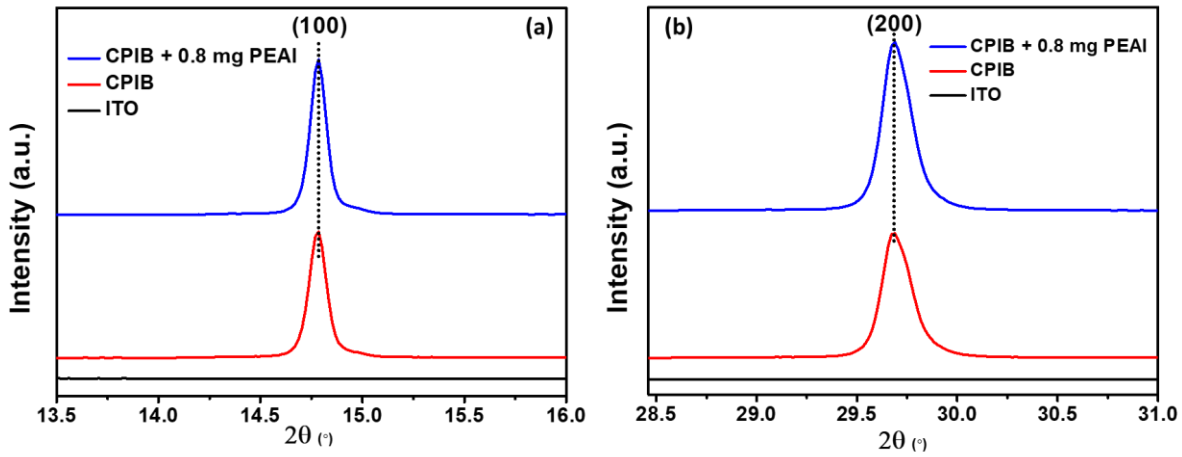

Fig. S4 Enlarged X-ray powder diffraction patterns corresponding to the (100) and (200) lattice planes of the CPIB and 0.8 mg PEAI assisted CPIB perovskite films.

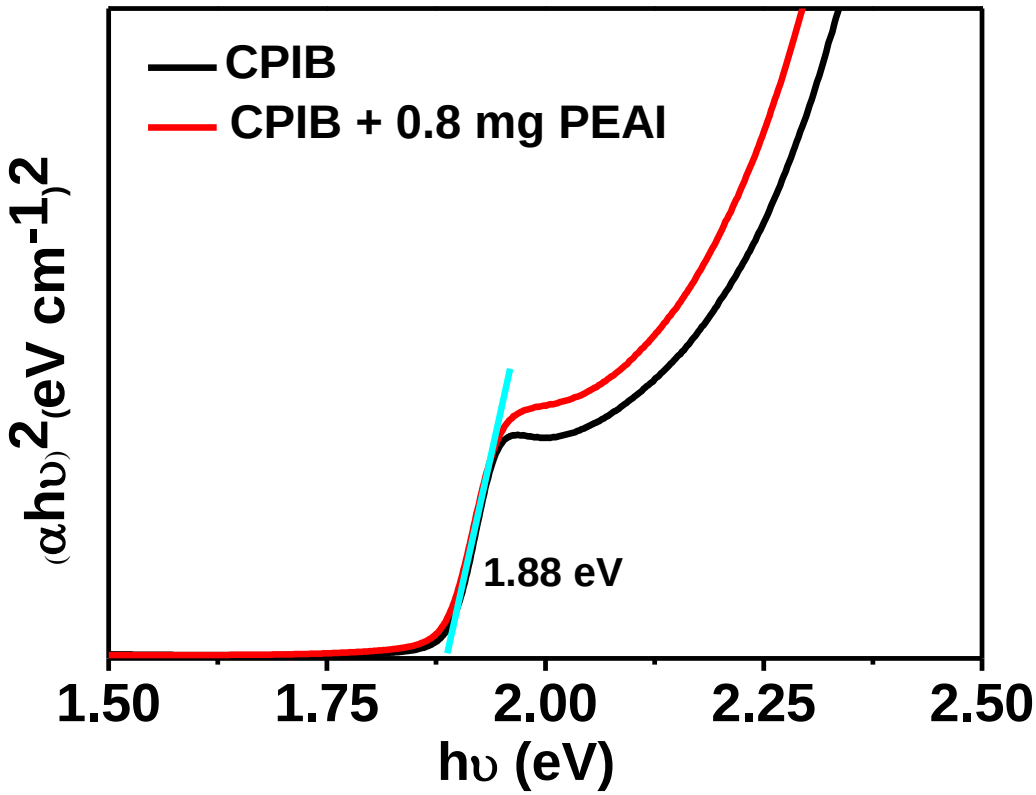

Fig. S5 Tauc plots of the CPIB and 0.8 mg PEAI assisted CPIB perovskite films.

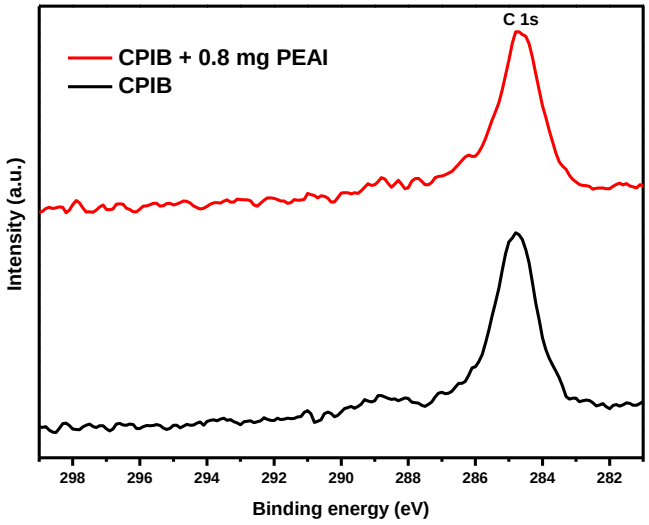

Fig. S6: High resolution C1s spectrum of CPIB and 0.8 mg PEAI CPIB films.

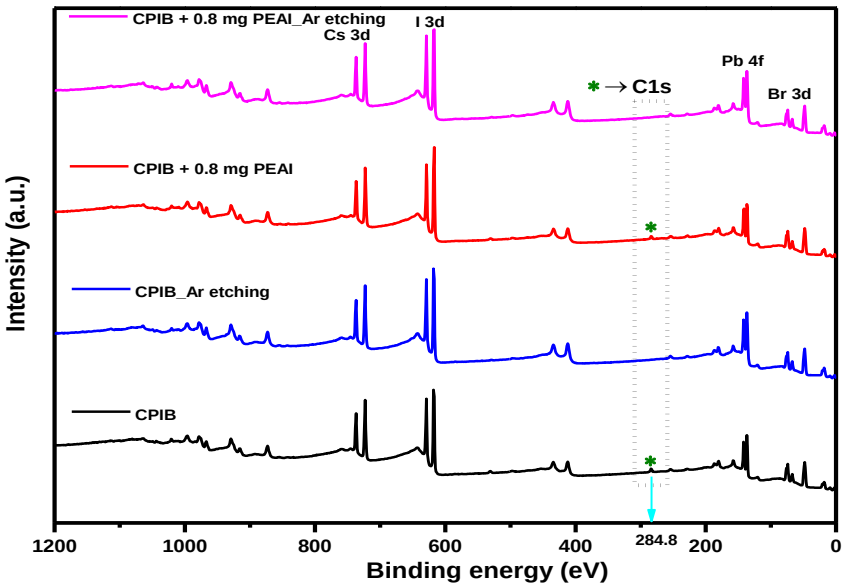

Fig. S7: XPS survey scan of CPIB and 0.8 mg PEAI CPIB films with surface as well as after surface treatment via Ar ion etching gun for 20 sec.

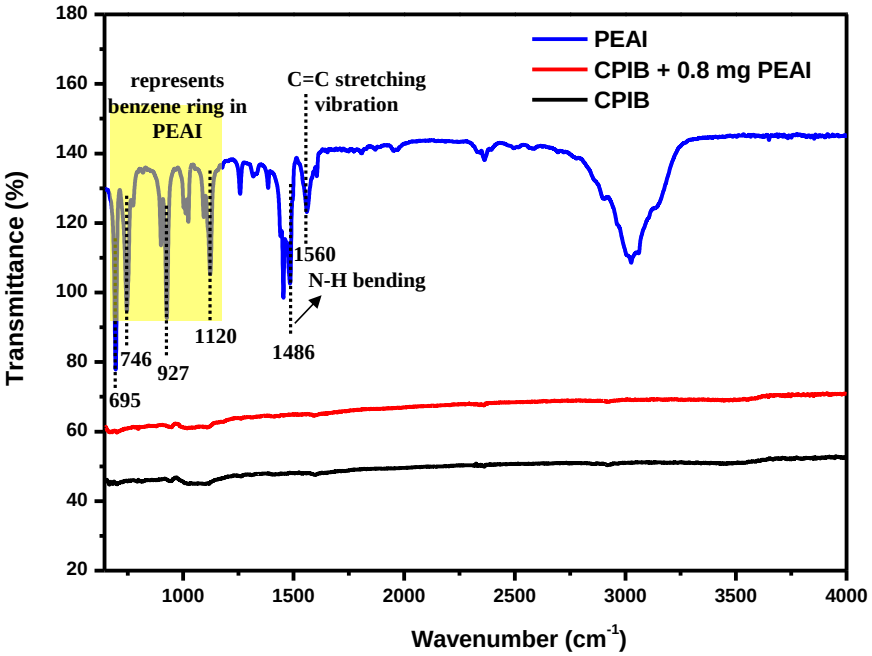

Fig. S8: FTIR spectrums for PEAI, CPIB and 0.8 mg + PEAI CPIB films.

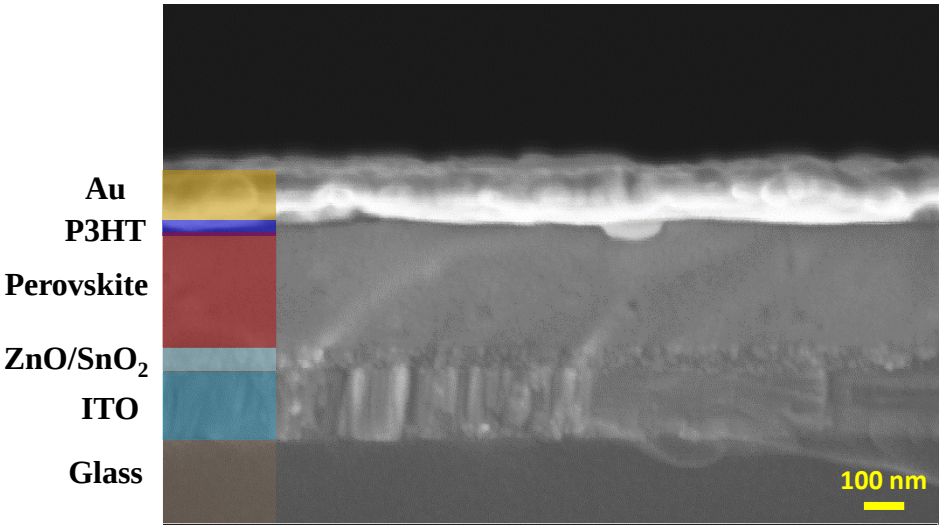

Fig. S9: Cross section FESEM image of cell.

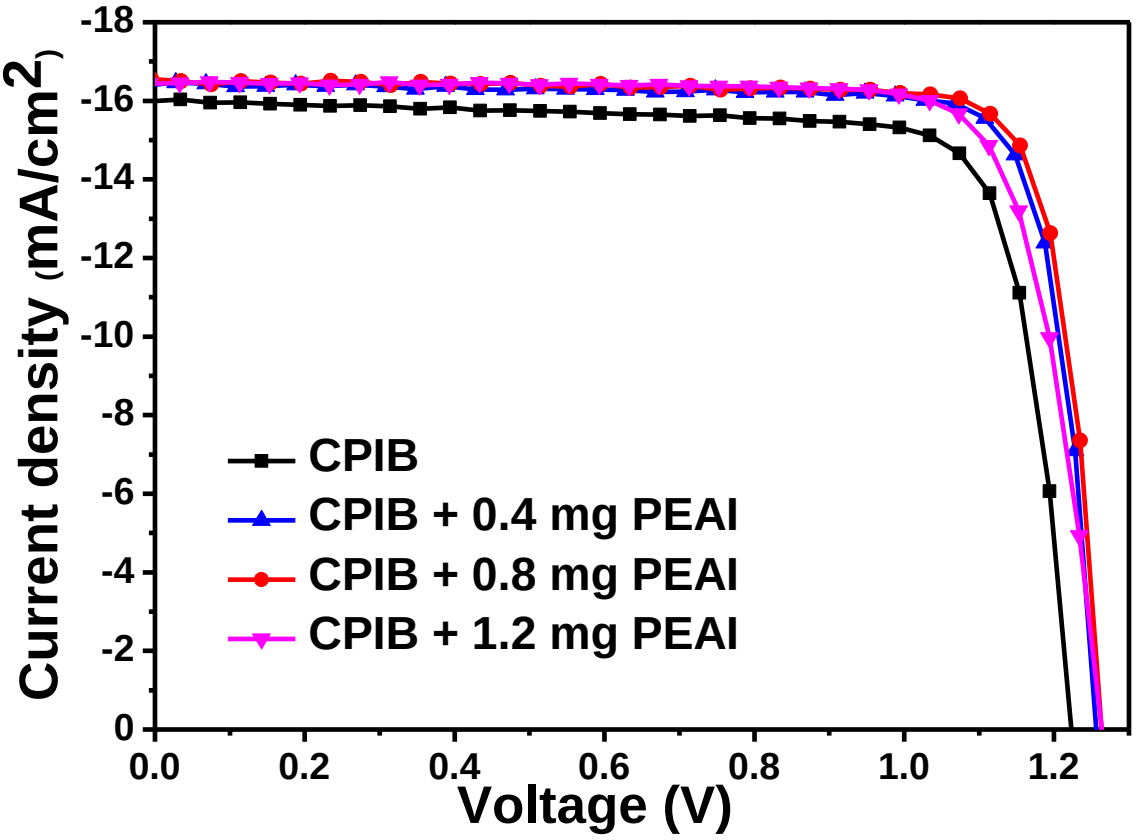

Fig. S10 Current-density (*J*-*V*) curves for the CPIB and 0.4, 0.8, and 1.2 mg PEAI assisted PSCs.

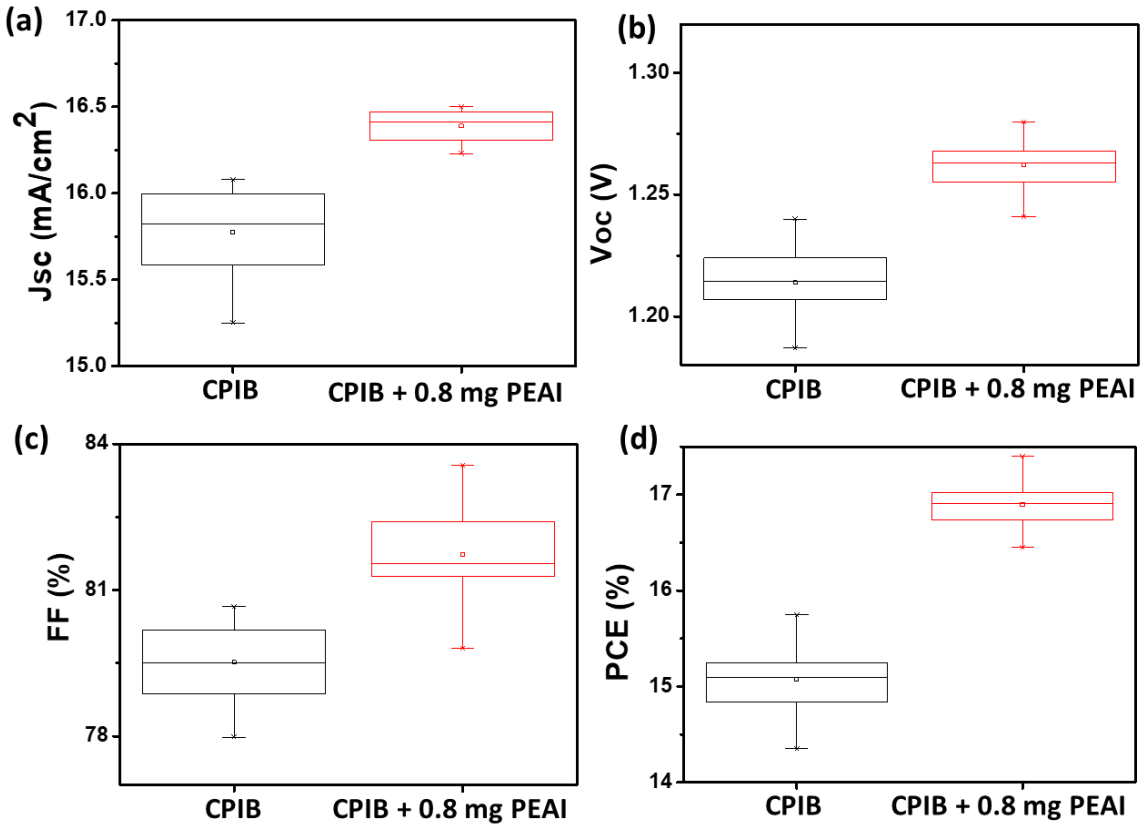

Figure S11. Photovoltaic parameter statistics analysis: (a) J_{SC}, (b), V_{OC} (c) FF, and (d) PCE for 20 independent PSCs of the CPIB and 0.8 mg PEAI assisted CPIB.

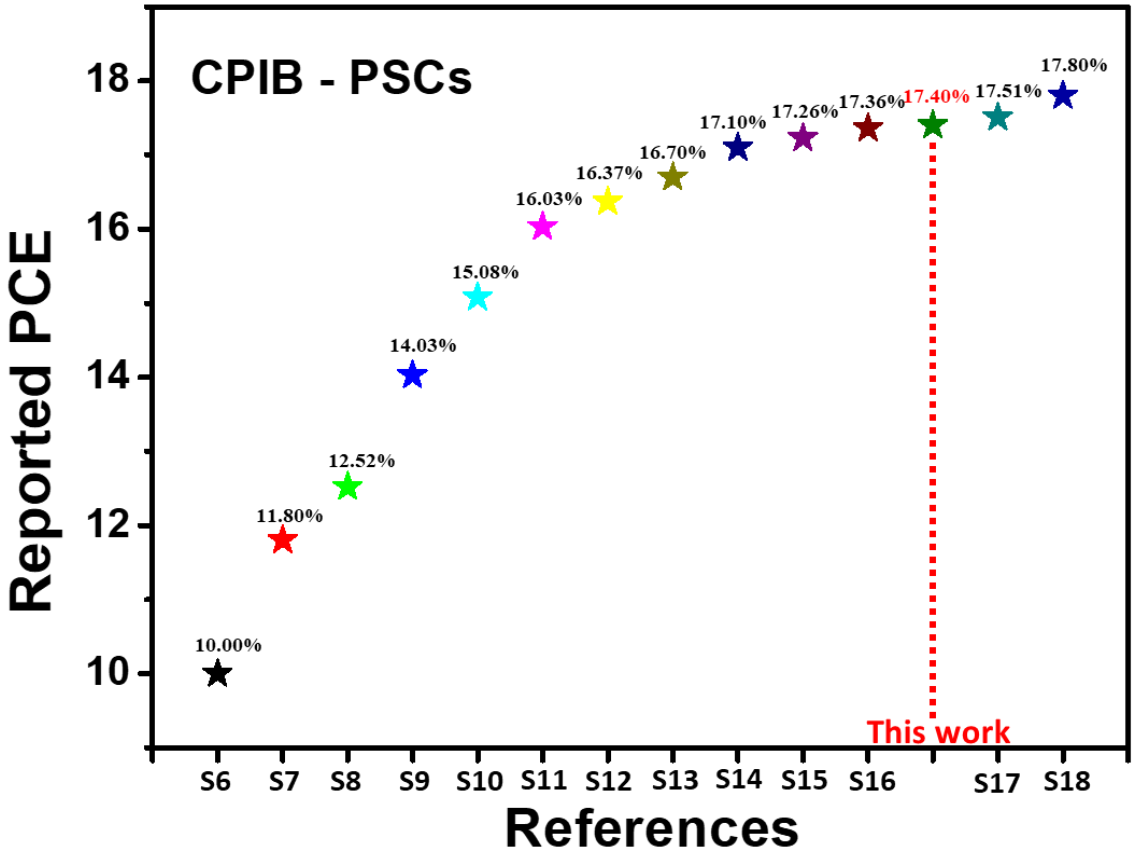

Figure S12. Summary of the high PCE for the reported CPIB based PSCs.

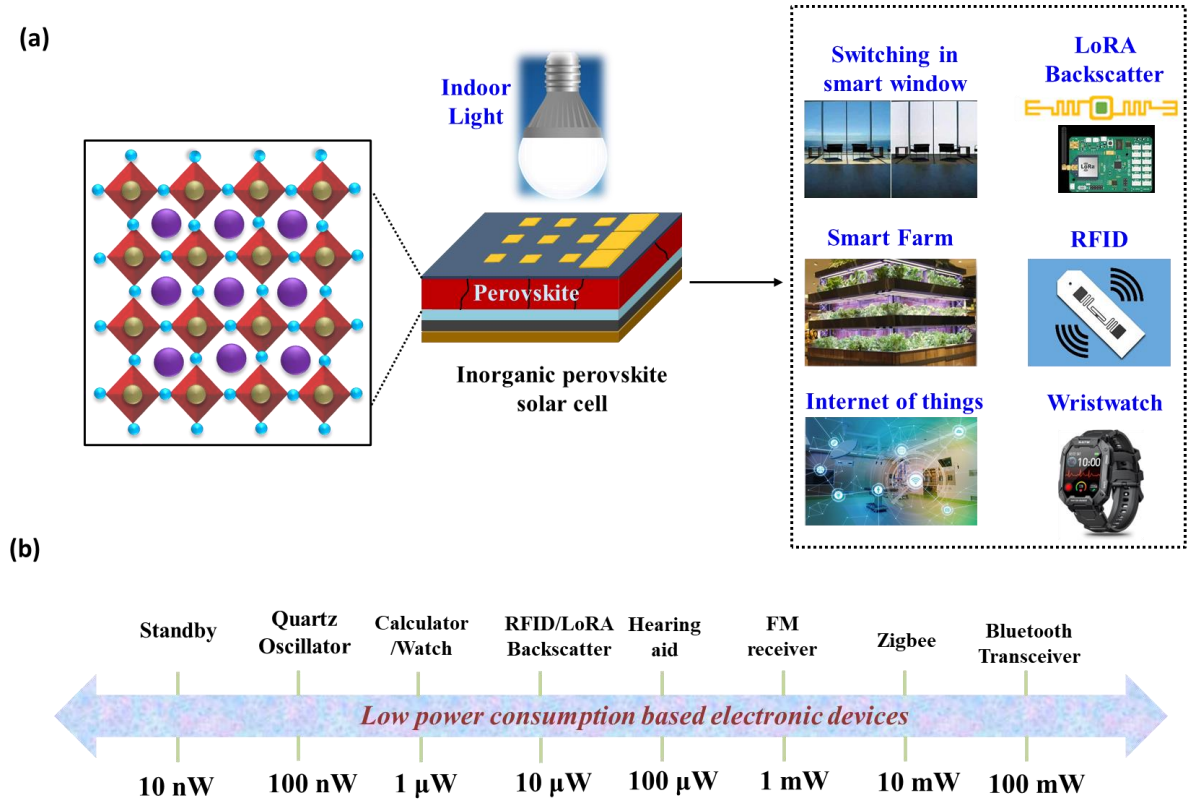

Figure S13. Schematic representation of (a) applications of Indoor PSCs, (b) power consumption for various modern electronic devices.

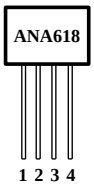

Pin No.	Pin Name	Pin Function
1	GND	Ground Pin
2	CE	Enable
3	LX	Switch pin
4	VDD	Input Power

Fig. S14: Pin diagram of ANA618 IC and corresponding pin descriptions.

Table S1 Reported $CsPbI_2Br$ (CPIB) based research works with PEAI.

Reference for $CsPbI_2Br$-device fabrication with PEAI & device structure	**Strategy**	**Novelty Description**	**Processing conditions**	**PCE (%)**
FTO/TiO_2/ perovskite/PTAA/Au [S19]	Surface passivation of $CsPbI_2Br$ (CPIB) film (Surface passivation strategy) (*2-step approach*)	Authors suggested that surface treatment of CPIB film with PEAI, reduced the trap states, improved the film quality.	Not mentioned	14.68
ITO/SnO_2/ZnO/ perovskite/passivation layer/carbon [S20]	Surface passivation of $CsPbI_2Br$ film (Surface passivation strategy) (*2-step approach*)	Authors demonstrated that PEAI was used as a passivation layer on top of CPIB perovskite film. The post treatment of PEAI reduced perovskite defects, leading to higher device performance.	N_2 filled glovebox	12.88
FTO/SnO_2/perovskite /carbon [S21]	Surface passivation of CPIB film (Surface passivation strategy) (2-step approach)	Authors suggested that PEAI surface treatment decreased the trap density, enhanced the CPIB film quality.	Not mentioned	13.38
FTO/TiO_2/perovskite /carbon [S22]	Surface passivation of $CsPbI_2Br$ film (Surface passivation strategy) (2-step approach)	Authors treated perovskite film surface with PEAI + ethylammonium iodide (EAI), and suggested that synergetic effect of PEAI+EAI effectively reduced the surface defects, decreased trap states, resulting increased film quality.	glovebox with dry air controlled at about 20% relative humidity	13.76
FTO/TiO_2/perovskite /spiro-OMeTAD/Ag [S23]	Surface passivation of CPIB film (Surface passivation strategy) (2-step approach)	Authors explored that PEAI treatment on the perovskite surface plays key role in the improvement of film quality.	Not mentioned	11.20

<This work>				
ITO/SnO_2/ZnO/ perovskite/P3HT/Au	**PEAI added into the perovskite precursor as an additive** **Additive Engineering** (In situ crystal reconstruction strategy) **(1-step approach)**	We proposed that PEAI additive into CPIB perovskite precursor plays a key role to modulate the crystallization process by forming intermediate phase. The PEAI additive controls the perovskite crystal growth, limits nuclei center, and retards the crystallization kinetics, result in improving the film quality.	**Ambient air**	**17.40**

Table S2 Crystal lattice parameters corresponding to (100) and (200) planes of the CPIB and 0.8 mg PEAI treated CPIB perovskite films.

Parameters	**Symbol**	CPIB **(100)**	CPIB + 0.8 mg PEAI **(100)**	CPIB **(200)**	CPIB + 0.8 mg PEAI **(200)**
Full width at half maximum (˚)	β	0.10088	0.093534	0.171413	0.16937
Peak angle (˚)	2θ	14.78514	14.78521	29.68805	29.68769
Average crystallite size (nm)	D	79.40964	85.64632	47.94595	48.52434
Strain	ε	0.160455	0.148771	0.13347	0.13188

Table S3 Photovoltaic parameters of the CPIB, 0.4, 0.8, and 1.2 mg PEAI additives based PSCs.

Devices		J_{SC} (mA/cm^2)	V_{OC} (mV)	*FF* (%)	*PCE* (%)
CPIB	Champion	16.03	1226	80.15	15.75
	Average	15.75 ± 0.25	1210 ± 15	79 ± 1.10	15.05 ± 0.65
CPIB + 0.4 mg PEAI	Champion	16.43	1259	83.16	17.20
	Average	16.20 ± 0.22	1244 ± 13	82.50 ± 0.65	16.62 ± 0.54
CPIB + 0.8 mg PEAI	Champion	16.47	1264	83.56	17.40
	Average	16.25 ± 0.20	1252 ± 10	83 ± 0.54	16.88 ± 0.46
CPIB + 1.2 mg PEAI	Champion	16.44	1255	81.48	16.81
	Average	16.15 ± 0.21	1238 ± 15	80.80 ± 0.65	16.18 ± 0.55

Table S4: Nyquist parameters of the CPIB and 0.8 mg PEAI based PSCs.

Parameters	CPIB	0.8 mg PEAI + CPIB
R_s (Ω)	29	26
R_{rec} (Ω)	4759	8745

References:

S1. Q. Hu, E. Rezaee, M. Li, Q. Chen, C. Li, S. Cai, H. Shan, Z. X. Xu,Sol. RRL 2020,**4**, 1900340

S2. M. Ulfa, T. Zhu, F. Goubard and T. Pauporté, *J. Mater. Chem. A*, 2018, **6**, 13350-13358.

S3. N. Yaghoobi Nia, E. Lamanna, M. Zendehdel, A. L. Palma, F. Zurlo, L. A. Castriotta and A. Di Carlo, *Small*, 2019, **15**, 1904399.

S4. M. Cai, V. T. Tiong, T. Hreid, J. Bell and H. Wang, *J. Mater. Chem. A*, 2015, **3**, 2784-2793.

S5. A. Isakova and P. D. Topham, *J. Polym. Sci., Part B: Polym. Phys.*, 2017, **55**, 549-568.

S6. J. K. Nam, S. U. Chai, W. Cha, Y. J. Choi, W. Kim, M. S. Jung, J. Kwon, D. Kim and J. H. Park, *Nano Lett.*, 2017, **17**, 2028.

S7. C. Y. Chen, H. Y. Lin, K. M. Chiang, W. L. Tsai, Y. C. Huang, C. S. Tsao and H. W. Lin, Adv. Mater., 2017, **29**, 1605290.

S8. L. Zhang, B. Li, J. Yuan, M. Wang, T. Shen, F. Huang, W. Wen, G. Cao and J. Tian, *J. Phys. Chem. Lett.*, 2018, **9**, 3646.

S9. F. Yu, Q. Han, L. Wang, S. Yang, X. Cai, C. Zhang and T. Ma, *Sol.*, 2021, **5**, 2100404.

S10. X. Yang, H. Yang, X. Hu, W. Li, Z. Fang, K. Zhang, R. Huang, J. Li, Z. Yang and Y. Song, *J. Mater. Chem. A*, 2020, **8**, 5308.

S11. W. Tang, Y. Chen, J. Yang, R. Yuan, Y. Lv, Q. Ma, Y. Wu, P. Zhang and W.-H. Zhang, *J. Power Sources*, 2021, **482**, 228965.

S12. Y. Zhang, C. Wu, D. Wang, Z. Zhang, X. Qi, N. Zhu, G. Liu, X. Li, H. Hu and Z. Chen, *Sol. RRL*, 2019, **3**, 1900254.

S13. J. He, J. Su, Z. Lin, J. Ma, L. Zhou, S. Zhang, S. Liu, J. Chang and Y. Hao, *Adv. Sci.*, 2021, **8**, 2101367.

S14. T. Ozturk, E. Akman, A. E. Shalan and S. Akin, *Nano Energy*, 2021, **87**, 106157.

S15. J. Xu, J. Cui, S. Yang, Z. Liu, X. Guo, Y. Che, D. Xu, W. Zhao, N. Yuan and J. Ding, *Adv. Funct. Mater.*, 2022, 2202829.

S16. Z. Guo, A. K. Jena, I. Takei, M. Ikegami, A. Ishii, Y. Numata, N. Shibayama and T. Miyasaka, *Adv. Funct. Mater.*, 2021, **31**, 2103614.

S17. X. Liu, H. Lian, Z. Zhou, C. Zou, J. Xie, F. Zhang, H. Yuan, S. Yang, Y. Hou and H. G. Yang, *Adv. Energy Mater.*, 2022, **12**, 2103933.

S18. Y. Ding, Q. Guo, Y. Geng, Z. Dai, Z. Wang, Z. Chen, Q. Guo, Z. Zheng, Y. Li and E. Zhou, *Nano Today*, 2022, **46**, 101586.

S19. H. Wang, H. Bian, Z. Jin, L. Liang, D. Bai, Q. Wang and S. F. Liu, *Sol. RRL*, 2018, **2**, 1800216.

S20. X. Zhang, D. Zhang, T. Guo, C. Zheng, Y. Zhou, J. Jin, Z. Zhu, Z. Wang, X. Cui and S. Wu, *J. Mater. Chem. C*, 2022, **10**, 15573-15581.

S21. Y. Wu, Q. Zhang, L. Fan, C. Liu, M. Wu, D. Wang and T. Zhang, *ACS Appl. Energy Mater.*, 2021, **4**, 5583-5589.

S22. X.-N. Huo, K.-X. Wang, R. Yin, W.-W. Sun, Y.-S. Sun, Y.-K. Gao, T.-T. You and P.-G. Yin, *Sol. Energy Mater. Sol. Cells*, 2022, **247**, 111963.

S23. C. Gao, Z. Hu, C. Yang, H. Xu, Y. Wang, H. Zhang, J. Zhang, Y. Zhu and J. Wang, *J. Alloys Compd.*, 2020, **848**, 156247.